







Ab initio investigation of charge density wave and superconductivity in two-dimensional Janus 2H/1T-MoSH monolayers

Ruiqi Ku ^{1,2,*}, Luo Yan ^{1,3,*}, Jian-Guo Si ⁴, Songyuan Zhu,⁵ Bao-Tian Wang ⁴, Yadong Wei ², Kaijuan Pang,² Weiqi Li,^{2,†} and Liujiang Zhou ^{1,3,‡}

¹*Yangtze Delta Region Institute (Huzhou), University of Electronic Science and Technology of China, Huzhou 313001, China*

²*School of Physics, Harbin Institute of Technology, Harbin 150001, China*

³*School of Physics, University of Electronic Science and Technology of China, Chengdu 610054, China*

⁴*Institute of High Energy Physics, Chinese Academy of Sciences, Beijing 100049, China*

⁵*Faculty of Innovation Engineering, Macau University of Science and Technology, Macau 999078, China*



(Received 26 August 2022; revised 7 January 2023; accepted 3 February 2023; published 21 February 2023)

Janus structures with the breaking of out-of-plane mirror symmetry have gained intensive attention. Here, on the basis of first principles, we not only investigate the recently discovered Janus 2H-MoSH monolayer [ACS Nano **15**, 20319 (2021)], but also report the global minimum structure of a Janus 1T-MoSH monolayer. Meanwhile, 2H-MoSH monolayer can easily transform into the 1T phase, overcoming a relatively small barrier of 0.13 eV. Intriguingly, Janus 1T-MoSH is a charge-density wave (CDW) material and its CDW order can be regulated via external strains. When Janus 1T-MoSH is subjected to 3% compressive strain, its CDW is completely suppressed and a superconducting state with a superconducting transition temperature T_c of 25.15 K emerges. Moreover, Janus 2H-MoSH monolayer is an intrinsic superconductor with a T_c of ~ 26.81 K and its T_c can be enhanced up to 36.69 K under a 1% tensile strain. Our work provides more in-depth insights for superconducting and CDW in low-dimensional transition metal dichalcogenides and related Janus systems.

DOI: [10.1103/PhysRevB.107.064508](https://doi.org/10.1103/PhysRevB.107.064508)

I. INTRODUCTION

Two-dimensional (2D) Janus transition metal dichalcogenides (TMDs) are an emerging generation of 2D systems with the lack of out-of-plane symmetry of the crystal structures. Compared with traditional TMD monolayers, 2D Janus TMDs show exotic properties, including strong Rashba spin splitting [1], sizable piezoelectric effects [2], second harmonic generation (SHG) response [3], and so forth, favoring their potential applications in various fields as ferrovalley materials [4], sensors [5], multiferroic materials [6], catalysts [7], optoelectronic devices [8], etc. Importantly, 2D Janus materials have been successfully fabricated mainly via selective epitaxial atomic replacement (SEAR) over the past decade, although they do not exist in nature [9,10]. The most typical example is the successful fabrication of Janus MoS₂ monolayer in the 2H phase, which was obtained by fully replacing the top S atoms layer by Se atoms in the original MoS₂ monolayer with thermal selenization methods [3,11]. Comparing with the MoS₂ or MoSe₂ monolayer, 2D Janus MoS₂Se owns its unique merits, such as a tunable intrinsic electric field to improve sensitivity for gas molecule adsorption [12], an intrinsic dipole to break the conventional limit of 1.23 eV in photocatalytic water splitting [13]. Thus building

2D materials with high asymmetry on two surfaces becomes a new kind of design technique at the atomic level.

Janus 2H-MoSH monolayer is an intermediate product in realizing Janus TMDs by involving stripping the top-layer S of MoS₂ with H atoms [3]. Very recently, it was confirmed during the synthesis of 2D Janus 2H-MoSSe via fully replacing the top S atoms layer in 2D MoS₂ with H atoms using gentle H₂-plasma treatment at room temperature [14]. It exhibits a metallic nature with a highly intrinsic carrier concentration [14]. In addition, this newly obtained 2D Janus 2H-MoSH has attracted widespread focus. Recently, it was predicted to be a strong conventional high-temperature 2D superconductor [15]. Furthermore, Janus 2H-MoSH can be considered as an efficient metallic contact to a MoSi₂N₄ semiconductor with high charge injection efficiency in MoSH/MoSi₂N₄ van der Waals (vdW) heterostructure, providing a new pathway for the design of optoelectronic applications [16]. However, due to the structural diversities in 2D TMDs [17] (e.g., 2H, 1T, 1T', and $2a \times 2a$ phases), thus only the Janus 2H-MoSH monolayer was studied in the past, which greatly limits sufficient understanding about the 2D Janus MoSH materials.

In this study, we systematically investigate the favorable Janus MoSH monolayers, namely 2D 2H- and 1T-MoSH, from their structure, electronic, mechanical, and superconducting properties. Here, Janus 2H-MoSH monolayer has been determined in experiment recently and Janus 2D 1T-MoSH is the most energetically favorable one, which we report in our present work. Meanwhile, 2H-MoSH monolayer can easily transform into the 1T phase with a relatively small phase transition barrier of 0.13 eV. Interestingly, 1T-MoSH

*These authors contributed equally to this work.

[†]tccliweiqi@hit.edu.cn

[‡]liujiang86@gmail.com

monolayer is a CDW material caused by electron-phonon coupling (EPC) interactions, which is confirmed by phonon spectrum and electron susceptibility calculations. Moreover, the CDW order in 1T-MoSH monolayer is highly sensitive to the electron temperature and external strains. Furthermore, 2D 1T-MoSH turns into a 2D superconductor with a high superconducting transition temperature $T_c = 25.15$ K when 3% compressive strain is applied. In addition, 2H-MoSH monolayer also exhibits a high $T_c \sim 26.81$ K, and its T_c can be further enhanced to 36.69 K when it is subjected to a biaxial tensile strain of 1%. Our present findings enrich the exploration of Janus MoSH families and pave an avenue for the controllable design of future nanomaterials.

II. COMPUTATIONAL DETAILS

Based on the density functional theory (DFT) framework, the first-principles calculations were performed through the Vienna ab initio simulation package (VASP) [18]. The generalized gradient approximation (GGA) [19] with the Perdew-Burke-Ernzerhof (PBE) exchange correlation functional and projector-augmented wave (PAW) pseudopotential were employed to simulate the interaction between the electrons and ions [20,21]. The cutoff energy for the plane-wave basis was set as 600 eV. $21 \times 21 \times 1$ k -point grid [22] was adopted for geometric optimization. To avoid the interactions of adjacent unit cells, a vacuum space in the nonperiodic direction was set to 20 Å. The convergence criterion of atomic relaxation was carried out 10^{-6} eV in total energy and all forces on each atom were 0.01 eV Å $^{-1}$. The optB88-vdw method was applied in order to correct for dispersion interactions [23]. The dipolar correction was included in Janus structural models. The phonon modes were further studied in the framework of density functional perturbation theory (DFPT), in which the second-order interatomic force constants were calculated based on harmonic approximation. Here, the $6 \times 6 \times 1$ supercell with 108 atoms and $3 \times 3 \times 1$ k point were utilized.

The EPC calculations were calculated via the QUANTUM ESPRESSO (QE) code [24]. The cutoff was set to 80 Ry for plane-wave kinetic energy and 320 Ry for the charge density. The k point with a Methfessel-Paxton smearing width of 0.02 Ry for electronic self-consistent calculations was sampled on $36 \times 36 \times 1$. The phonon modes were computed within DFPT on $6 \times 6 \times 1$ q meshes, which is in agreement with the result obtained from VASP calculations (Fig. 8). According to the Migdal-Eliashberg theory [25], the magnitude of the EPC λ_{qv} can be calculated by

$$\lambda_{qv} = \frac{\gamma_{qv}}{\pi \hbar N(E_F) \omega_{qv}^2}, \quad (1)$$

where γ_{qv} is the phonon linewidth, ω_{qv} is the phonon frequency, and $N(E_F)$ is the density of states (DOS) at the Fermi level. The γ_{qv} can be estimated by

$$\gamma_{qv} = \frac{2\pi\omega_{qv}}{\Omega_{\text{BZ}}} \sum_{k,n,m} |g_{\text{kn},k+qm}^v|^2 \delta(\epsilon_{kn} - \epsilon_F) \delta(\epsilon_{k+qm} - \epsilon_F), \quad (2)$$

where Ω_{BZ} is the volume of Brillouin zone (BZ), ϵ_{kn} and ϵ_{k+qm} denote the Kohn-Sham energy, and $g_{\text{kn},k+qm}^v$ represents

the EPC matrix element. The $g_{\text{kn},k+qm}^v$ can be determined self-consistently by the linear response theory. The Eliashberg electron-phonon spectral function $\alpha^2 F(\omega)$ [26] and the cumulative frequency dependence of EPC $\lambda(\omega)$ can be calculated by

$$\alpha^2 F(\omega) = \frac{1}{2\pi N(E_F)} \sum_{qv} \frac{\gamma_{qv}}{\omega_{qv}} \delta(\omega - \omega_{qv}) \quad (3)$$

and

$$\lambda(\omega) = 2 \int_0^\omega \frac{\alpha^2 F(\omega')}{\omega'} d\omega', \quad (4)$$

respectively. Using a typical value of the effective screened Coulomb repulsion constant $\mu^* = 0.1$ [27–29] as well as the Eliashberg spectral function $\alpha^2 F(\omega)$ and λ , one can calculate the logarithmic average frequency ω_{log} by

$$\omega_{\text{log}} = \exp \left[\frac{2}{\lambda} \int_0^\infty \frac{d\omega}{\omega} \alpha^2 F(\omega) \log \omega \right]. \quad (5)$$

Finally, the T_c can be derived by the full Allen-Dynes formula [30]

$$T_c = f_1 f_2 \frac{\omega_{\text{log}}}{1.2} \exp \left[-\frac{1.04(1 + \lambda)}{\lambda - \mu^*(1 + 0.62\lambda)} \right], \quad (6)$$

with

$$f_1 f_2 = \sqrt[3]{1 + \left(\frac{\lambda}{2.46(1 + 3.8\mu^*)} \right)^2} \times \left(1 - \frac{\lambda^2 (1 - \frac{\omega_2}{\omega_{\text{log}}})}{\lambda^2 + 3.312(1 + 6.3\mu^*)^2} \right), \quad (7)$$

where $f_1 f_2$ is a correction term and ω_2 is the mean-square frequency,

$$\omega_2 = \sqrt{\frac{1}{\lambda} \int_0^{\omega_{\text{max}}} \left[\frac{2\alpha^2 F(\omega)}{\omega} \right] \omega^2 d\omega}. \quad (8)$$

In addition, the cutoff energy and k points used in our VASP and QE simulations had been tested to guarantee an energy convergence of less than 1 meV per formula unit (Fig. 9).

III. RESULTS AND DISCUSSION

A. Structure, electronic, and mechanical properties

Typically, due to the different coordination modes of transition metal atoms, 2D TMDs usually have 2H, 1T, 1T', and $2a \times 2a$ phases. Therefore, similar to 2D TMDs, Janus MoSH monolayer also can exist above typical structures. In this work, we only focus on Janus 2H- and 1T-MoSH monolayers, due to the kinetic instabilities of Janus 1T' and $2a \times 2a$ MoSH monolayers. Specifically, the energy of 1T-MoSH monolayer is lower by 67.7 meV per atom than that of 2H phase. This is inverse to the case in Janus MoSSe, in which the 2H phase is more energetically stable than the 1T one [31]. More discussions are presented in the Appendix materials. As shown in Figs. 1(a) and 1(d), 2D 1T- and 2H-MoSH crystallize in a hexagonal lattice and have a space group of $P3M1$ (No. 156), corresponding to the C_{3V} point symmetry. For 1T-MoSH monolayer, the hydrogen atoms are not in the perpendicular

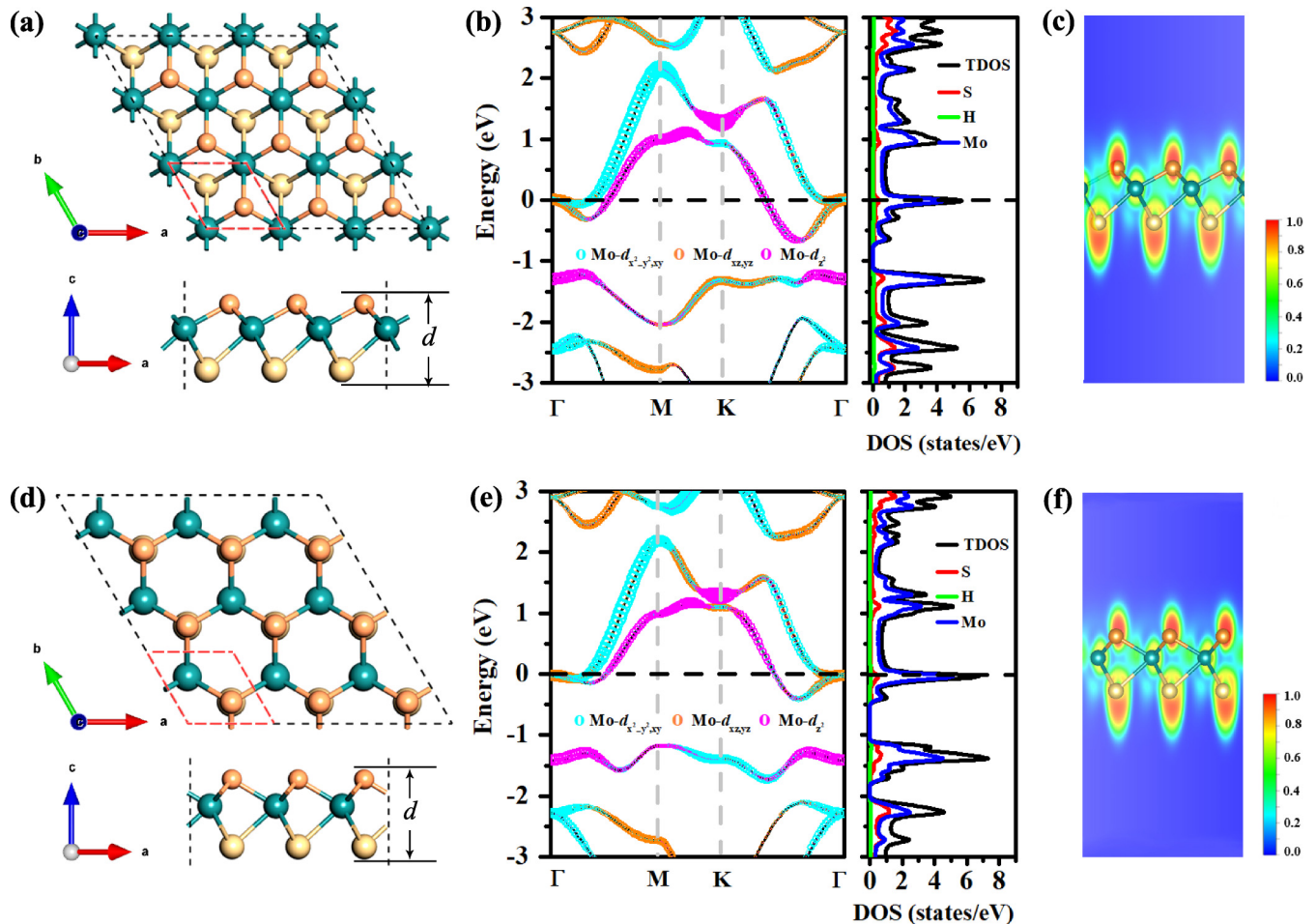


FIG. 1. (a/d) Geometric configuration from top and side views, (b/e) the projected band structure and density of states (DOS), and (c/f) ELF plots for 1T-/2H-MoSH monolayer. The Fermi level is set to be zero. The Mo, S, and H atoms are marked in green, white, and orange, respectively.

direction of sulfur atoms, while the hydrogen atoms locate in the vertical direction of sulfur atoms in 2D 2H-MoSH. The optimized lattice constants of 1T-MoSH monolayer are $a = b = 3.05 \text{ \AA}$ and the layer thickness is $d = 2.58 \text{ \AA}$. The Mo – H and Mo – S bond lengths are 2.01 and 2.38 \AA , respectively. As for 2H-MoSH monolayer, the lattice constant a is 3.03 \AA , which is consistent with previous experimental and theoretical values [14,16]. The layer spacing is enlarged to 2.67 \AA due to the larger Mo – H bonds (2.04 \AA). The electron localization function (ELF) is a conventional approach to analyze bonding characteristics, which is described as

$$ELF = \frac{1}{1 + (D/D_h)}, \quad (9)$$

$$D = \frac{1}{2} \sum_i |\nabla \varphi_i|^2 - \frac{1}{8} \frac{|\nabla \rho|^2}{\rho}, \quad (10)$$

$$D_h = \frac{3}{10} (3\pi^2)^{5/3} \rho^{5/3}. \quad (11)$$

The φ_i refer to the Kohn-Sham orbitals and $\rho = \sum_i |\varphi_i|^2$ represents electron charge density. The value range of ELF is in between 0 and 1. $ELF = 1$ corresponds to perfect localization of electrons and 0.5 indicates a uniform electron gas [32,33]. As depicted in Figs. 1(c) and 1(f), the Mo – H and Mo – S

bonds in 1T- and 2H-MoSH monolayers have mainly ionic bonding features. Moreover, as the atomic-resolved band structures shown in Figs. 1(b) and 1(e), MoSH monolayers exhibit metallic behavior with two bands crossing the Fermi level and their metallic behavior is mainly dominated by the correlative states from Mo- d orbitals.

There are three independent elastic constants in hexagonal Janus 1T/2H-MoSH monolayers and the calculated values are presented in Table I. Clearly, both Janus 1T- and 2H-MoSH systems are mechanically stable, satisfying the criteria for 2D hexagonal crystal: $C_{11} > |C_{12}|$ and $C_{66} > 0$ [34]. Besides, the elastic properties of homogeneous and isotropic materials can be evaluated by two independent constants—Young's modulus Y and Poisson's ratio ν [35,36]. The Y along the x and y directions can be defined as

$$Y_x = (C_{11}C_{22} - C_{12}C_{21})/C_{22}, \quad (12)$$

$$Y_y = (C_{11}C_{22} - C_{12}C_{21})/C_{11}. \quad (13)$$

Moreover, the ν is the ratio of the transverse strain to the axial strain, which can be estimated by

$$\nu_x = C_{12}/C_{22}, \quad (14)$$

$$\nu_y = C_{12}/C_{11}. \quad (15)$$

TABLE I. Optimized lattice constants (a/b), the layer thickness (d), Bader charges on the Mo atoms (Q_{Mo}), elastic constants (C_{ij}), Young's modulus (Y), and Poisson's ratios (ν) for MoSH monolayers.

System	2H-MoSH	1T-MoSH
$a = b$ (Å)	3.03	3.05
d (Å)	2.67	2.58
Q_{Mo} ($ e $)	0.95	1.06
$C_{11} = C_{22}$ (N/m)	127.66	100.49
C_{12} (N/m)	37.66	38.51
C_{66} (N/m)	45.00	30.99
Y_x/Y_y (N/m)	116.55	85.73
ν_x/ν_y	0.29	0.38

In light of the isotropy, the in-plane Y in x and y directions are equal. The evaluated Y values for 1T- and 2H-MoSH monolayers are 85.73 and 116.55 N/m, respectively, which are lower than that of MoS₂ (160.12 ± 7.85 N/m) [37] and other 2D flexible materials, i.e., borophene (210 N/m) [38] and graphene (350 N/m) [39]. These results indicate that Janus 2D 1T- and 2H-MoSH have great potential applications in flexible materials, especially for 1T-MoSH monolayer. On the other hand, the ν values of 2H and 1T systems are 0.29 and 0.38, respectively. In general, the ν value below 0.5 implies this material possesses some compressibility [40]. Moreover, in respect of bond characters, $\nu = 0.25$ means the inflection point from ionicity to metallicity. Therefore, the bond types in 2D 1T- and 2H-MoSH are mainly ionic, which is in line with former discussions. Furthermore, Bader charge analysis suggests that the Mo atom acts as an electron donor and the electrons transfer from the Mo to S and H atoms. As listed in Table I, the electrons transfer ability in 2D 1T-MoSH is stronger than that in 2H-MoSH monolayer.

B. 2H to 1T structural transition

The *ab initio* molecular dynamics (AIMD) simulations at 300 K are performed for 1T- and 2H-MoSH monolayers. Their energy fluctuations within 10 ps along with the final configurations are shown in Fig. 10 (in the Appendix materials). Clearly, the energy fluctuations of 1T-MoSH monolayer remain nearly constant during the entire simulation period and no structural reconstruction occurs after 10 ps, suggesting its thermal stability at 300 K. However, for 2H-MoSH monolayer, a large energy fluctuation appears at ~ 0.5 ps, and the structure is nearly stabilized to a 1T configuration and lasting to the end of the simulation period. Therefore, 2D 2H-MoSH has the tendency to transform to the 1T phase when a small energy was applied.

In the following, we will discuss the structural transition in MoSH monolayer by utilizing the climbing image nudged elastic band method [41]. As shown in Fig. 2, the energy barrier for the structural transition from 2H- to 1T-MoSH monolayer is about 0.13 eV (0.04 eV/atom), which is highly smaller than that in MoS₂ (0.52 eV/atom) [17], indicating the experimental feasibility of structural transition from 2H- to 1T-MoSH monolayer under appropriate environments.

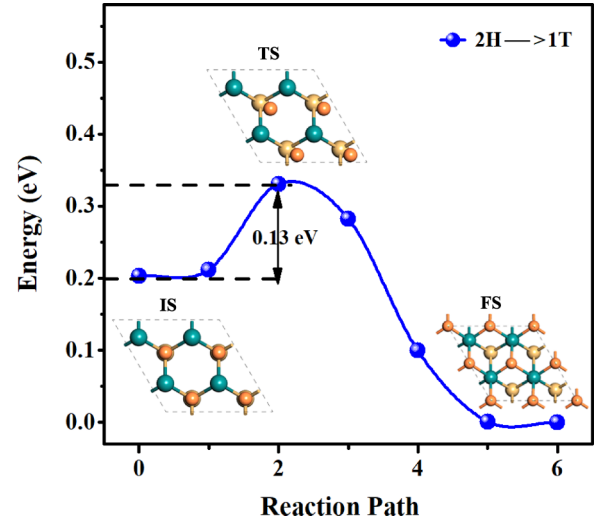


FIG. 2. Energy barrier of phase transition from 2H-MoSH to 1T-MoSH monolayer, including the atomic configurations of initial state (IS), transition state (TS), and final state (FS).

C. CDW and superconductivity in 1T-MoSH monolayer

There are two evident Kohn anomalies in phonon spectrum along the high symmetry paths for 1T-MoSH monolayer and the imaginary mode locates at the M point [Fig. 3(a)]. Such behavior in phonon spectrum is a classic phenomenon for CDW materials. As we know, the critical smearing parameter σ , which represents the electronic temperature and has been widely used in the electronic self-consistent calculations to accelerate the convergence, smears out the abrupt change of the Fermi-Dirac statistics in the ground state [42–44]. By changing this parameter, one can qualitatively assess the effect of electronic temperature on the CDW transition. To determine whether the imaginary phonon modes are regulated by the σ , the phonon dispersions of the 2D 1T-MoSH under several σ values are calculated and are exhibited in Fig. 3(a). Results

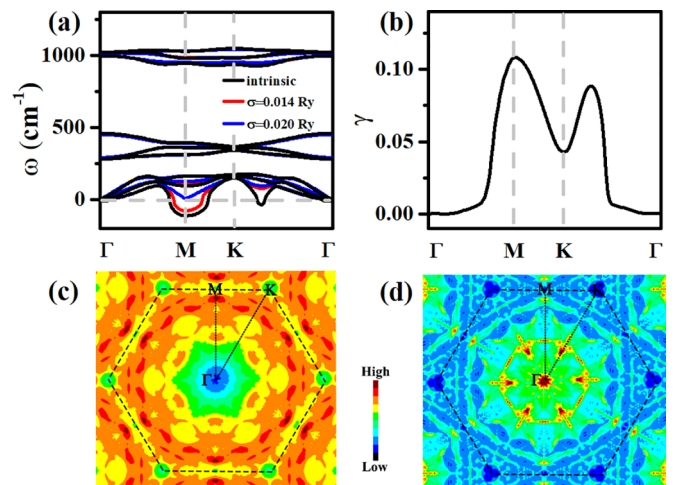


FIG. 3. (a) Phonon dispersions subjected to Fermi-Dirac smearing widths. (b) The phonon linewidth of the lowest mode of intrinsic 1T-MoSH. (c) Real part and (d) imaginary part of the electronic susceptibility for intrinsic 1T-MoSH monolayer.

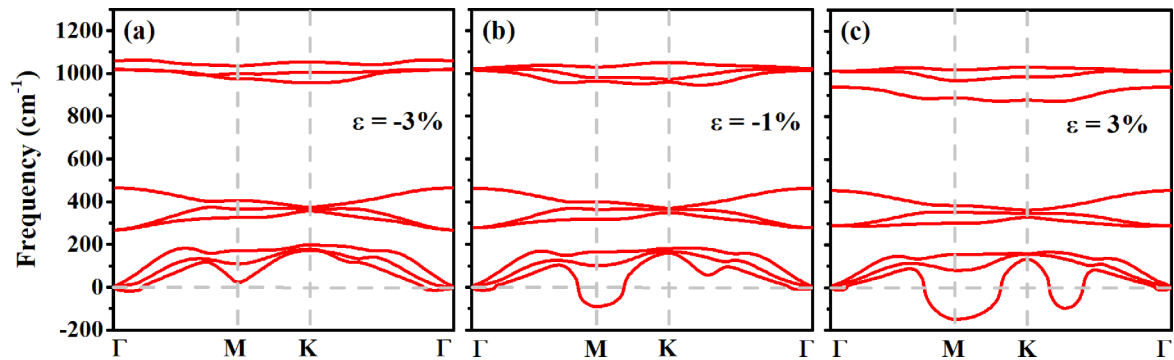


FIG. 4. Phonon dispersion curves of 1T-MoSH monolayer under the compressive strain of (a) 3%, (b) 1%, and (c) tensile strain of 3%.

indicate that the imaginary phonon dispersion is strongly dependent on the electron temperature and the negative phonon modes can be lifted along with the increase of σ and then completely change to be a positive phonon mode with $\sigma = 0.020$ Ry. This situation is highly similar to the CDW transitions in 1T-TaSe₂ [45] and 1T-TiSe₂ [42] monolayers, in which the negative phonon modes also occur at the M point. Therefore, Janus 1T-MoSH is predicted to be a 2D CDW material and the imaginary phonon mode at the M point implies a commensurate CDW phase transition reconstructed structure.

The origin of CDW has been much complicated till now and there is no unified mechanism to explain it in different CDW materials. Here, we discuss two typical aspects, Fermi-surface nesting (FSN) and EPC, as the potential driving forces in the formation of CDW order for 2D 1T-MoSH. The concept of CDW was first proposed by Peierls [46], in order to describe a fundamental instability of a one-dimensional (1D) metal chain. The key feature of Peierls' model is FSN, which is well defined as the superposition of Fermi surfaces when translated one to another by a nesting vector \mathbf{q} in electronic structure. The Lindhard susceptibility function is a crucial method to reflect the FSN, which can be given by its real and imaginary parts [47]

$$\text{Re}[\chi_0(\vec{q}, \omega)] = \frac{2}{(2\pi)^2} \int_{\text{BZ}} d\vec{k} \frac{f_{\vec{k}} - f_{\vec{k}+\vec{q}}}{\omega + \varepsilon_{\vec{k}} - \varepsilon_{\vec{k}+\vec{q}}}, \quad (16)$$

$$\text{Im}[\chi_0(\vec{q}, \omega)] = \frac{1}{2\pi} \int_{\text{BZ}} d\vec{k} (f_{\vec{k}} - f_{\vec{k}+\vec{q}}) \delta(\omega + \varepsilon_{\vec{k}} - \varepsilon_{\vec{k}+\vec{q}}), \quad (17)$$

where ω is the field frequency, ε is the electron's energy, and f denotes the electron's Fermi distribution function. The transition momentum is conserved with $\vec{k} + \vec{q} = \vec{k}'$. The Gaussian function as smearing function with a dense $129 \text{ \AA} \times 129 \text{ \AA} \times 1$ k -point grid was used to calculate the Lindhard function using the measured band structure. This further derives the electron susceptibilities. Generally speaking, the real part reflects the stability of the electronic system and usually induces CDW in the system when divergence occurs, while the imaginary part reveals the real topological information of the Fermi surface. If the origin of CDW in a system is dominated by FSN, then both the real part and imaginary part of the Lindhard susceptibility function are required to have a peak at the CDW wave vector [48]. In the case of

Janus 1T-MoSH, Figs. 3(c) and 3(d) show that the strongest peaks in the real part of the electronic susceptibility occur near the M point, while the peak of the imaginary part is along the Γ -K direction, with no visible peak at the M point. The difference in the peak locations between the real and imaginary parts of electron susceptibility function eliminates FSN as the driving force for the formation of CDW in 1T-MoSH monolayer. For real materials, when the noninteracting Lindhard function cannot properly represent the properties of the electronic system [49], the momentum-dependent EPC needs to be further considered to explain the phonon mode softening and CDW origin. The phonon linewidth γ of the lowest vibrational mode of 1T-MoSH monolayer reflects the strength of the EPC directly. Clearly shown in Fig. 3(b), two peaks locate in the entire BZ, the main peak being at the M point and another peak occurring along the K - Γ path. Meanwhile, the location with the highest value is in accord with the results of phonon dispersions. Therefore, the formation of the CDW order in 1T-MoSH monolayer is attributed to the momentum-dependent EPC effect [50].

To explore the evolution of the CDW order under external strains, the phonon dispersions of 1T-MoSH monolayer upon a series of biaxial strains ranging from -3% to 3% are presented in Fig. 4. Obviously, the compressive strain also can lift the imaginary phonon frequencies [Figs. 4(a) and 4(b)] and the intrinsic imaginary frequencies at the M point become positive when the compressive strain reaches to 3%, indicating that the 1T phase tends to be stabilized under compressive strain. In contrast, the tensile strain can weaken the phonon frequencies and largely expand the area of instability at the CDW vector [Fig. 4(c)]. All in all, the CDW phase and normal states in 1T-MoSH monolayer can be effectively tuned via suitable strains.

Subsequently, we evaluate the influence of electronic temperature on CDW order. Note that the smearing parameter σ is used in the DFT calculations via a Fermi-Dirac distribution function to reflect the electronic temperature. A smaller smearing value corresponds to a smaller electronic temperature [51]. Significantly, the electron temperature is not equivalent to the real temperature and cannot directly compare to the real temperature applied to the material. The electron temperature is proportional to the real temperature to a certain extent, but is much larger than it. Nevertheless, it is still significant to evaluate CDW properties of materials based on electron temperature alone. The CDW transition temperature

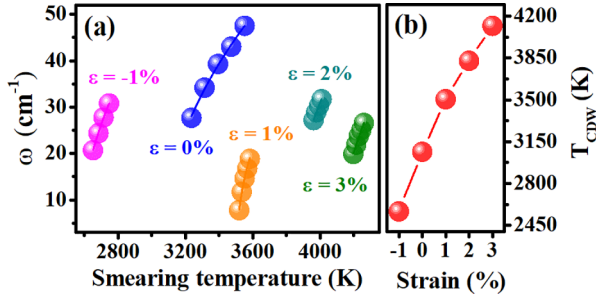


FIG. 5. (a) Phonon frequencies of softened acoustic mode at the M point as a function of the electronic temperature under biaxial compressive and tensile strains. (b) Fitted CDW transition temperatures under compressive and tensile strains.

of Janus 1T-MoSH can be obtained according to the following function [52]

$$\omega_M(T) = \omega_0 * (T - T_{CDW})^\delta, \quad (18)$$

where ω_M is the phonon frequency at the M point, T is the smearing electron temperature, T_{CDW} is the CDW transition temperature, and δ is the exponent, varying from 0.48 to 0.53 for different meshes, which is quite close to the value of 0.5 for mean-field models.

The fitted smearing electron temperature dependence of phonon frequencies at the M point is shown in Fig. 5(a) and the obtained T_{CDW} as a function of biaxial strain is plotted in Fig. 5(b). Some fitting parameters are also listed in Table II. Clearly, the T_{CDW} becomes higher along with the larger tensile strain, further demonstrating that the tensile strain can enhance the CDW order. Thus the control of strain is useful to manipulate the CDW transition, which may open a promising prospect in the future to construct controllable switching electronic devices.

When the CDW order is suppressed, the superconductivity may be induced in the Janus 1T-MoSH monolayer. As reported in the former, the CDW instability is completely eliminated under 3% biaxial compressive strain. Here, we thus study the superconductivity in 1T-MoSH monolayer under compressive strain of 3%. The decomposition of the phonon

TABLE II. Fitting parameters of CDW transition temperature.

Strain	T_{CDW} (K)	ω_0 (cm ⁻¹)	δ
-1%	2568	2.06	0.52
0%	3069	2.19	0.50
1%	3508	2.42	0.48
2%	3828	2.32	0.50
3%	4119	2.36	0.49

spectrum with respect to the vibration directions of Mo, S, and H atoms is shown in Fig. 6(a). Evidently, the vibration of the H atoms occupies the high-frequency region, near 1000 cm⁻¹. This is because the phonon vibration frequency is inversely proportional to the square root of the element mass. Then S atoms occupy the midfrequency range of 200–500 cm⁻¹, while the Mo atoms locate below 200 cm⁻¹. These distributions are consistent with the projected phonon density of states (PhDOS) in Fig. 6(b). Due to the evident softened phonon mode at the M point and mainly contributed from the in-plane Mo atomic vibrations, this mode phonon accounts for 91.6% of the total EPC ($\lambda = 2.37$) [Fig. 6(c)]. As a consequence, $\lambda(\omega)$ increases rapidly in this range, leading to the largest peak of the $\alpha^2F(\omega)$. For a system with strong EPC interactions, it is necessary to introduce a correction term when evaluating the superconducting temperature, as shown in Eq. (6). In this way, according to the full Allen-Dynes formula [16,53], the superconducting transition temperature of 1T-MoSH is estimated to be 25.15 K. The T_c of Janus 1T-MoSH monolayer is much larger than those experimentally reported T_c values for 2D materials, such as LiC₆ (5.9 K) [54] and C₆CaC₆ (4.0 K) [55]. Our results clearly indicate that the compressive strain can suppress the CDW transition and induce superconductivity in Janus 1T-MoSH monolayer.

D. Superconductivity in 2H-MoSH monolayer

In order to better compare the superconducting properties between Janus 1T- and 2H-MoSH monolayers, we next characterize the superconductivity of 2D 2H-MoSH. The

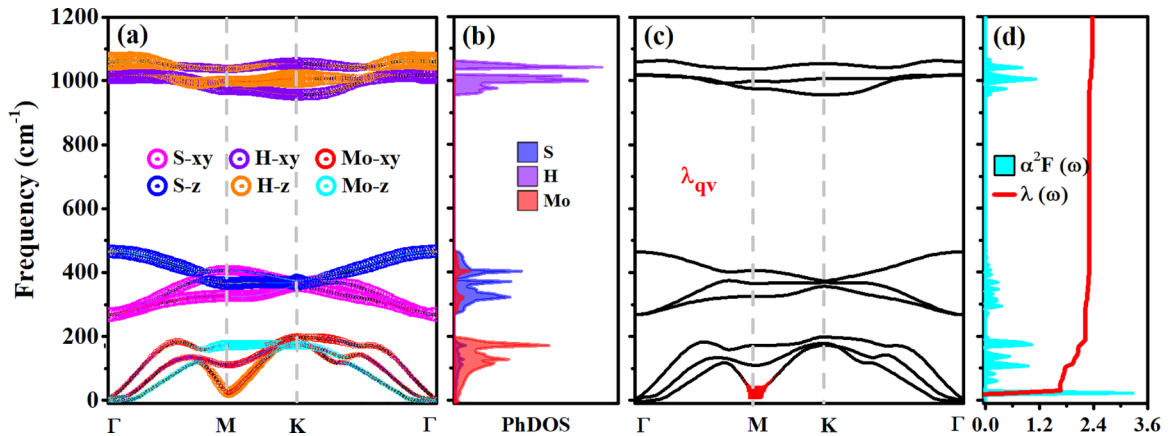


FIG. 6. When 3% compressive strain was applied to 1T-MoSH monolayer: (a) the phonon spectrum weighted by the eigenvalues of vibration modes of Mo, S, and H atoms; (b) phonon density of states (PhDOS) for 2D 1T-MoSH; (c) the magnitude of the EPC λ_{qv} ; (d) the Eliashberg spectral function $\alpha^2F(\omega)$ and the cumulative contribution to the EPC strength $\lambda(\omega)$.

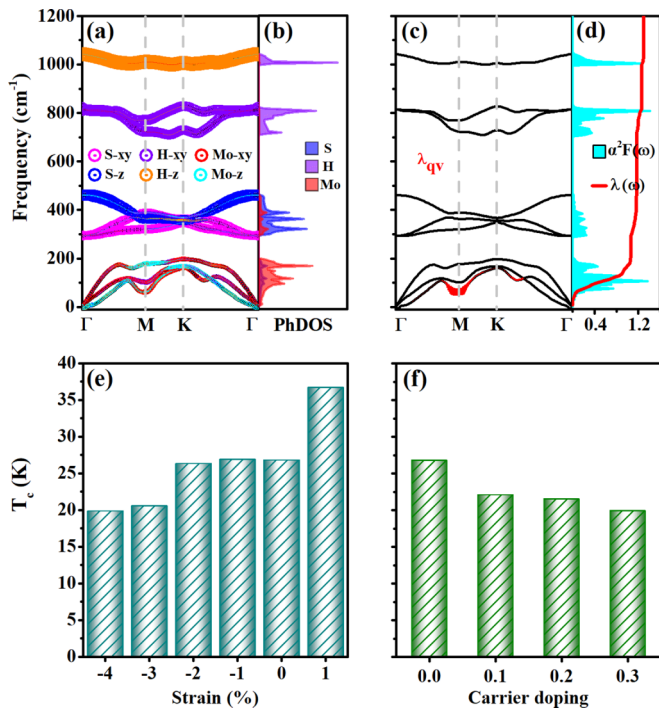


FIG. 7. (a) Phonon spectrum of 2H-MoSH monolayer, projected by the vibration modes of Mo, S, and H atoms and (b) PhDOS. (c) The magnitude of the EPC λ_{qv} . (d) The Eliashberg spectral function $\alpha^2F(\omega)$ and the cumulative contribution to the EPC strength $\lambda(\omega)$. The variations of T_c as a function of (e) biaxial strains and (f) carrier doping.

decomposed phonon spectrum and PhDOS are shown in Figs. 7(a) and 7(b), respectively, clearly favoring that the Janus 2H-MoSH monolayer is dynamically stable. Figure 7(c) shows that the relatively large strength of the EPC (labeled by λ_{qv}) is related to the soft mode in the first acoustic branch, stemming from the Mo-xy vibrations. Thus it makes a significant contribution to the cumulative frequency-dependent EPC function $\lambda(\omega)$, evidencing the jump of the total EPC in this range and accounting for 80.8% of the total EPC intensity ($\lambda = 1.27$), while the S and H atoms, dominating the optical branches, contribute the remaining EPC, $\sim 19.2\%$. Finally, the T_c of 2H-MoSH monolayer is evaluated to be 26.81 K, which is comparable to the former reported value (28.92 K in 2D 2H-MoSH) [15] and is higher than many reported 2D

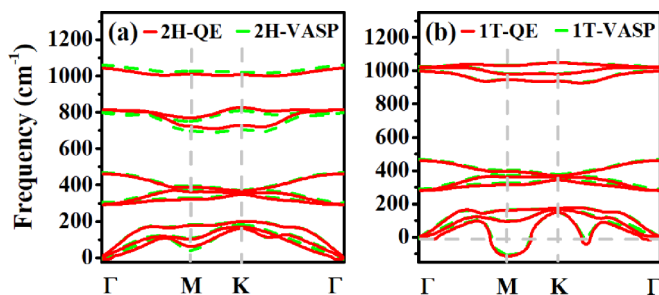


FIG. 8. Phonon spectra of (a) 2H and (b) 1T phases for MoSH monolayers based on VASP and QE calculations. The VASP and QE calculations on phonon spectra almost show the same dispersion, indicating their validations in this work.

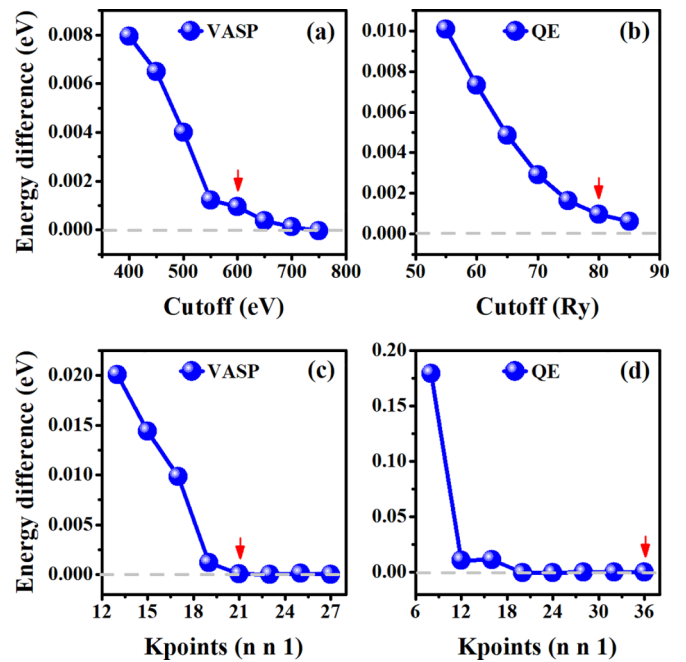


FIG. 9. Calculated energy difference as a function of (a/b) cutoff energy and (c/d) k points for VASP/QE calculations. The value pointed by the red arrow was the convergent parameters that were used in simulations.

TMD superconductors, such as WS_2 (8.8 K) [56], $(WS_2)_2Ca$ (9.3 K), and $(MoS_2)_2Ca$ (13.3 K) [57]. Indeed, the softened phonon mode in low-frequency phonons is the main factor for this strong EPC in the Janus 2H-MoSH monolayer.

Generally, 2D materials are prepared on the appropriate substrates, which would inevitably induce strain and doping effects. Hence the strain engineering and carrier doping have been adopted to modulate the superconducting properties for various 2D materials, such as $NiTe_2$ [58], B_2O [59], $1H-TaSi_2N_4$ [60], and so forth. Here, the superconductivities of Janus 2H-MoSH monolayer are also further explored when subjected to different external strains and carrier dopings. In Fig. 7(e), Janus 2H-MoSH monolayer remains kinetically

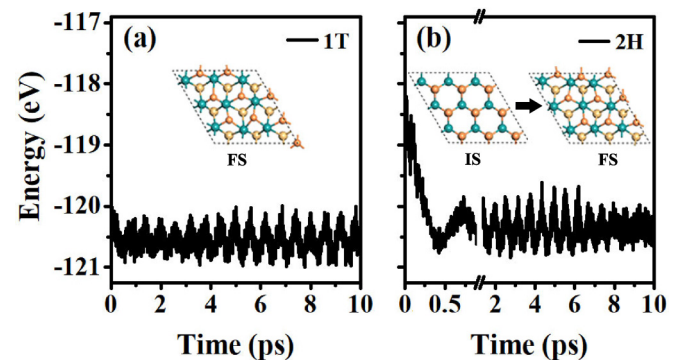


FIG. 10. (a/b) Variations of the energy of Janus 1T-/2H-MoSH monolayer within the AIMD simulations at 300 K. Intriguingly, 2H-MoSH shows a large energy fluctuation in the beginning 0.5 ps. The insets indicate the snapshots of initial state (IS) and final state (FS) during simulation period.

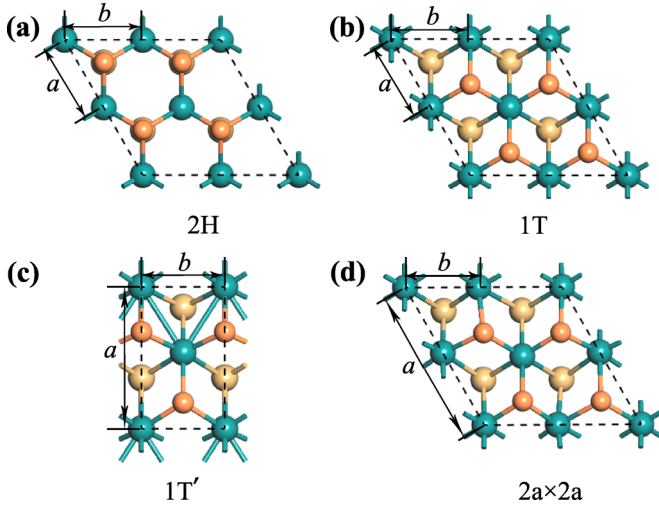


FIG. 11. Atomic structures of the (a) 2H, (b) 1T, (c) 1T', and (d) $2a \times 2a$ phases of MoSH monolayers.

stable with the strains ranging from -4% to 1% . We only optimize the atomic coordinates after each strain is applied. The compressive strain has a negative feedback on the T_c , while the tensile strain of 1% leads to the maximum value of 36.69 K. Beyond this critical strain, the stability of the Janus 2H-MoSH system is destroyed along with increasing the tensile strain. For the carrier doping case, we only focused on the effect of p -type doping on 2D Janus 2H-MoSH, because the slightly larger n -type doping (0.1 e/cell) gives rise to dynamical instability. Within a compensating uniform charge background, the p -type doping was simulated by directly removing electrons from the system and then fully relaxing the lattice and atomic positions. In Fig. 7(f), T_c decreases monotonically with hole doping. Apparently, p -type doping cannot improve the T_c of Janus 2H-MoSH. The same situation has also been confirmed in Cu_2Si monolayer [27]. Although we fail to modulate the T_c to a higher level by carrier doping, we theoretically provide clues for future experimental determinations. (See Table III.)

IV. CONCLUSIONS

In summary, we have performed systematic investigations on possible 2D Janus MoSH crystals and the Janus 1T- and

TABLE III. Superconductive parameters of $N(E_F)$ (in unit of states per spin per Ry per cell), ω_{log} (in K), λ , and T_c (in K) calculated by the full Allen-Dynes formula for Janus MoSH monolayers.

Systems	$N(E_F)$	ω_{log}	λ	T_c
1T	8.82	54.74	2.37	25.15
2H	10.10	197.58	1.27	26.81
2H (-4% strain)	8.94	253.96	0.91	19.88
2H (-3% strain)	9.33	222.84	0.99	20.57
2H (-2% strain)	10.19	218.85	1.17	26.32
2H (-1% strain)	10.06	216.89	1.20	26.89
2H (1% strain)	10.33	55.55	3.43	36.69
2H (0.1h/cell)	9.14	218.78	1.05	22.10
2H (0.2h/cell)	8.78	210.86	1.05	21.53
2H (0.3h/cell)	8.35	171.40	1.12	19.94

TABLE IV. Lattice parameters and total energy of per unit cell for various phases of monolayer MoSH.

Phase	a (\AA)	b (\AA)	E (eV)
2H	3.03	3.03	-13.4240
1T	3.05	3.05	-13.6273
1T'	5.25	3.09	-13.6466
$2a \times 2a$	6.15	2.84	-13.6469

2H-MoSH monolayers are the two most stable phases. Then, their structures, stability, electronic, and superconducting properties are fully investigated via the first-principles calculations. Unexpectedly, synthesized 2H-MoSH monolayer can easily lead to a structural transition with a small energy barrier of 0.13 eV, bringing a different CDW material, namely 2D 1T-MoSH. This is because the Janus 1T-MoSH monolayer is the energy global minimum structure in the 2D MoSH family. Moreover, the strong EPC interaction is the key factor for the origin of the CDW states in 1T-MoSH monolayer. The CDW order can be enhanced in the presence of tensile strain, while the compressive strain could suppresses it. Similar behavior can be drawn in the evolution of electron temperature. When 3% compressive strain is applied, the CDW states of the 1T-MoSH monolayer are completely eliminated and then the 1T-MoSH monolayer becomes a 2D superconductor with a high T_c of 25.15 K. In addition, 2H-MoSH shows a large $T_c \sim 26.81$ K and its T_c can be enhanced to a maximum value of 36.69 K upon applying an in-plane tensile strain of 1% . Thus Janus MoSH monolayers are high-temperature superconducting candidates, either in 1T or 2H phases. Our findings enrich the comprehension among different phases of Janus MoSH and will provide inspiration for further research on other 2D Janus TMD materials. (See also Figs. 8–10.)

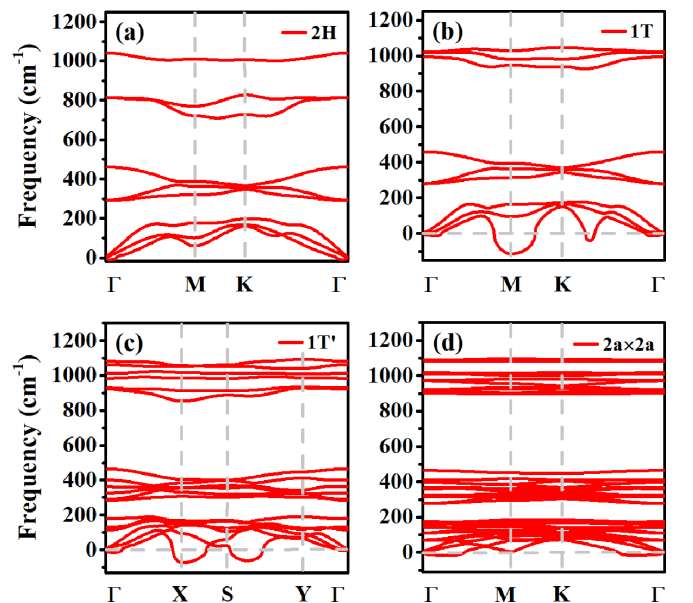


FIG. 12. Phonon spectra of (a) 2H, (b) 1T, (c) 1T', and (d) $2a \times 2a$ phases for possible MoSH monolayers.

ACKNOWLEDGMENTS

This work is supported by the Startup funds of Outstanding Talents of UESTC (Grant No. A1098531023601205), National Youth Talents Plan of China (Grant No. G05QNQR049), and the Open-Foundation of Key Laboratory of Laser Device Technology, China North Industries Group Corporation Limited (Grant No. KLLDT202106) W.Q.L. acknowledges the National Natural Science Foundation of China (Grant No. 11974091).

APPENDIX

2D TMDs usually exist in a variety of phases due to their unique layered structures and weak interlayer van der

Waals interactions. In our present studies, four typically distinct phases among 2D TMDs are further considered in Janus MoSH monolayers, as shown in Fig. 11. Their structural parameters and energies are listed in Table IV. According to their phonon spectra (Fig. 12), only the 2H-MoSH monolayer is dynamically stable at first glance. However, $1T'$ and $2a \times 2a$ phases have imaginary frequencies in the high-symmetry paths, showing their dynamic instabilities; therefore, they are no longer considered in the following works. Although a special imaginary frequency appears at M point in the $1T$ -MoSH monolayer, it is a classic phenomenon for possible CDW material. From another aspect, the $1T$ -MoSH monolayer is more energetically favorable than the $2H$ phase. Thus we fully study the $1T$ - and $2H$ -MoSH monolayers in our work.

- [1] S.-B. Yu, M. Zhou, D. Zhang, and K. Chang, *Phys. Rev. B* **104**, 075435 (2021).
- [2] L. Dong, J. Lou, and V. B. Shenoy, *ACS Nano* **11**, 8242 (2017).
- [3] A.-Y. Lu, H. Zhu, J. Xiao, C.-P. Chuu, Y. Han, M.-H. Chiu, C.-C. Cheng, C.-W. Yang, K.-H. Wei, Y. Yang *et al.*, *Nat. Nanotechnol.* **12**, 744 (2017).
- [4] Y.-F. Zhao, Y.-H. Shen, H. Hu, W.-Y. Tong, and C.-G. Duan, *Phys. Rev. B* **103**, 115124 (2021).
- [5] P. Panigrahi, D. Jini, H. Bae, H. Lee, R. Ahuja, and T. Hussain, *Appl. Surf. Sci.* **542**, 148590 (2021).
- [6] C. Zhang, Y. Nie, S. Sanvito, and A. Du, *Nano Lett.* **19**, 1366 (2019).
- [7] W. Chen, Y. Qu, L. Yao, X. Hou, X. Shi, and H. Pan, *J. Mater. Chem. A* **6**, 8021 (2018).
- [8] X. Yang, D. Singh, Z. Xu, Z. Wang, and R. Ahuja, *J. Mater. Chem. C* **7**, 12312 (2019).
- [9] D. B. Trivedi, G. Turgut, Y. Qin, M. Y. Sayyad, D. Hajra, M. Howell, L. Liu, S. Yang, N. H. Patoary, H. Li *et al.*, *Adv. Mater.* **32**, 2006320 (2020).
- [10] Y. Qin, M. Sayyad, A. R.-P. Montblanch, M. S. G. Feuer, D. Dey, M. Blei, R. Sailus, D. M. Kara, Y. Shen, S. Yang *et al.*, *Adv. Mater.* **34**, 2106222 (2022).
- [11] J. Zhang, S. Jia, I. Kholmanov, L. Dong, D. Er, W. Chen, H. Guo, Z. Jin, V. B. Shenoy, L. Shi *et al.*, *ACS Nano* **11**, 8192 (2017).
- [12] C. Jin, X. Tang, X. Tan, S. C. Smith, Y. Dai, and L. Kou, *J. Mater. Chem. A* **7**, 1099 (2019).
- [13] X. Ma, X. Wu, H. Wang, and Y. Wang, *J. Mater. Chem. A* **6**, 2295 (2018).
- [14] X. Wan, E. Chen, J. Yao, M. Gao, X. Miao, S. Wang, Y. Gu, S. Xiao, R. Zhan, K. Chen *et al.*, *ACS Nano* **15**, 20319 (2021).
- [15] P.-F. Liu, F. Zheng, J. Li, J.-G. Si, L. Wei, J. Zhang, and B.-T. Wang, *Phys. Rev. B* **105**, 245420 (2022).
- [16] C. V. Nguyen, C. Q. Nguyen, S.-T. Nguyen, Y. S. Ang, and N. V. Hieu, *J. Phys. Chem. Lett.* **13**, 2576 (2022).
- [17] H. L. Zhuang, M. D. Johannes, A. K. Singh, and R. G. Hennig, *Phys. Rev. B* **96**, 165305 (2017).
- [18] G. Kresse and J. Furthmüller, *Comput. Mater. Sci.* **6**, 15 (1996).
- [19] J. P. Perdew, K. Burke, and M. Ernzerhof, *Phys. Rev. Lett.* **77**, 3865 (1996).
- [20] P. E. Blöchl, *Phys. Rev. B* **50**, 17953 (1994).
- [21] G. Kresse and D. Joubert, *Phys. Rev. B* **59**, 1758 (1999).
- [22] H. J. Monkhorst and J. D. Pack, *Phys. Rev. B* **13**, 5188 (1976).
- [23] J. c. v. Klimeš, D. R. Bowler, and A. Michaelides, *Phys. Rev. B* **83**, 195131 (2011).
- [24] P. Giannozzi, S. Baroni, N. Bonini, M. Calandra, R. Car, C. Cavazzoni, D. Ceresoli, G. L. Chiarotti, M. Cococcioni, I. Dabo *et al.*, *J. Phys.: Condens. Matter* **21**, 395502 (2009).
- [25] F. Giustino, *Rev. Mod. Phys.* **89**, 015003 (2017).
- [26] P. B. Allen and R. C. Dynes, *Phys. Rev. B* **12**, 905 (1975).
- [27] L. Yan, P.-F. Liu, T. Bo, J. Zhang, M.-H. Tang, Y.-G. Xiao, and B.-T. Wang, *J. Mater. Chem. C* **7**, 10926 (2019).
- [28] M. Gao, Q.-Z. Li, X.-W. Yan, and J. Wang, *Phys. Rev. B* **95**, 024505 (2017).
- [29] L. Yan, J. Zhu, B.-T. Wang, J. He, H.-Z. Song, W. Chu, S. Tretiak, and L. Zhou, *Nano Lett.* **22**, 5592 (2022).
- [30] W. L. McMillan, *Phys. Rev.* **167**, 331 (1968).
- [31] X. Tang, S. Li, Y. Ma, A. Du, T. Liao, Y. Gu, and L. Kou, *J. Phys. Chem. C* **122**, 19153 (2018).
- [32] B. Silvi and A. Savin, *Nature (London)* **371**, 683 (1994).
- [33] A. Savin, R. Nesper, S. Wengert, and T. F. Fässler, *Angew. Chem. Int. Ed. Engl.* **36**, 1808 (1997).
- [34] F. Mouhat and F.-X. Coudert, *Phys. Rev. B* **90**, 224104 (2014).
- [35] C. D. Reddy, S. Rajendran, and K. M. Liew, *Nanotechnology* **17**, 864 (2006).
- [36] Q. Yue, J. Kang, Z. Shao, X. Zhang, S. Chang, G. Wang, S. Qin, and J. Li, *Phys. Lett. A* **376**, 1166 (2012).
- [37] Y. Li, C. Yu, Y. Gan, P. Jiang, J. Yu, Y. Ou, D.-F. Zou, C. Huang, J. Wang, T. Jia *et al.*, *npj Comput. Mater.* **4**, 49 (2018).
- [38] Z. Zhang, Y. Yang, E. S. Penev, and B. I. Yakobson, *Adv. Funct. Mater.* **27**, 1605059 (2017).
- [39] T. Jiang, R. Huang, and Y. Zhu, *Adv. Funct. Mater.* **24**, 396 (2014).
- [40] P. Mott, J. Dorgan, and C. Roland, *J. Sound Vib.* **312**, 572 (2008).
- [41] G. Mills, H. Jónsson, and G. K. Schenter, *Surf. Sci.* **324**, 305 (1995).
- [42] B.-T. Wang, P.-F. Liu, J.-J. Zheng, W. Yin, and F. Wang, *Phys. Rev. B* **98**, 014514 (2018).
- [43] Y. Ge and A. Y. Liu, *Phys. Rev. B* **82**, 155133 (2010).
- [44] J.-A. Yan, R. Stein, D. M. Schaefer, X.-Q. Wang, and M. Y. Chou, *Phys. Rev. B* **88**, 121403(R) (2013).

- [45] M. J. Wei, W. J. Lu, R. C. Xiao, H. Y. Lv, P. Tong, W. H. Song, and Y. P. Sun, *Phys. Rev. B* **96**, 165404 (2017).
- [46] R. E. Peierls, *Quantum Theory of Solids* (Oxford University Press, Oxford, 2001).
- [47] X. Zhu, J. Guo, J. Zhang, and E. Plummer, *Adv. Phys-X* **2**, 622 (2017).
- [48] M. D. Johannes and I. I. Mazin, *Phys. Rev. B* **77**, 165135 (2008).
- [49] X. Zhu, Y. Cao, J. Zhang, E. W. Plummer, and J. Guo, *Proc. Natl. Acad. Sci. U.S.A.* **112**, 2367 (2015).
- [50] J.-G. Si, W.-J. Lu, Y.-P. Sun, P.-F. Liu, and B.-T. Wang, *Phys. Rev. B* **105**, 024517 (2022).
- [51] N. D. Mermin, *Phys. Rev.* **137**, A1441 (1965).
- [52] D. L. Duong, M. Burghard, and J. C. Schön, *Phys. Rev. B* **92**, 245131 (2015).
- [53] J. Bardeen, L. N. Cooper, and J. R. Schrieffer, *Phys. Rev.* **108**, 1175 (1957).
- [54] J.-J. Zheng and E. R. Margine, *Phys. Rev. B* **94**, 064509 (2016).
- [55] S. Ichinokura, K. Sugawara, A. Takayama, T. Takahashi, and S. Hasegawa, *ACS Nano* **10**, 2761 (2016).
- [56] Y. Fang, J. Pan, D. Zhang, D. Wang, H. T. Hirose, T. Terashima, S. Uji, Y. Yuan, W. Li, Z. Tian *et al.*, *Adv. Mater.* **31**, 1901942 (2019).
- [57] R. Szcześniak, A. P. Durajski, and M. W. Jarosik, *Front. Phys.* **13**, 137401 (2018).
- [58] R. Ku, L. Yan, K. Xue, J. Zhang, K. Pang, M. Sha, B.-T. Wang, Y. Jiang, L. Zhou, and W. Li, *J. Phys. Chem. C* **126**, 6925 (2022).
- [59] L. Yan, P.-F. Liu, H. Li, Y. Tang, J. He, X. Huang, B.-T. Wang, and L. Zhou, *npj Comput. Mater.* **6**, 94 (2020).
- [60] L. Yan, B.-T. Wang, X. Huang, Q. Li, K. Xue, J. Zhang, W. Ren, and L. Zhou, *Nanoscale* **13**, 18947 (2021).